ACKNOWLEDGMENTS

We thank Dr. Robert S. Hellman and Dr. Gary Sayed for critical reading. We also thank Dr. Hülya Ellidokuz for statistical assistance, Özden Ülker and Türkan Ertay for preparing radiopharmaceuticals and Ismail Evren for his technical assistance.

This study was presented as an oral presentation at the European Association of Nuclear Medicine Congress, 1996.

REFERENCES

1. Tufo HM, Ostfeld AM, Shekelle R. Central nervous system dysfunction following open-heart surgery. *JAMA* 1970;212:1333–1340.
2. Branthwaite MA. Neurological damage related to open-heart surgery. *Thorax* 1972; 27:748–753.
3. Savageau JA, Stanton BA, Jenkins CD, Frater WM. Neuropsychological dysfunction following elective cardiac operation. *J Thorac Cardiovasc Surg* 1982;84:595–600.
4. Shaw PJ, Bates D, Cartlidge NEF, et al. Neurological complications of coronary artery bypass graft surgery: six-month follow-up study. *BMJ* 1986;293:165–167.
5. Smith PL. The cerebral complications of coronary artery bypass surgery. *Ann Royal Coll Surg* 1988;70:212–216.
6. Hammeke TA, Hastings JE. Neuropsychologic alterations after cardiac operations. *J Thorac Cardiovasc Surg* 1988;96:326–331.
7. Branthwaite MA. Detection of neurological damage during open-heart surgery. *Thorax* 1973;28:464–472.
8. Townes BD, Bashein G, Hombein TF, et al. Neurobehavioral outcomes in cardiac operations. *J Thor Cardiovasc Surg* 1989;98:774–782.
9. Strenge H, Lindner V, Paulsen G, Regensburger D, Tiemann S. Early neurological abnormalities following coronary artery bypass surgery. *Eur Arch Psychiatr Neurol Sci* 1990;239:277–281.
10. Sakakibara Y, Shiihara H, Terada Y, Ino T, Wanibuchi Y, Furuta S. Central nervous system damage following surgery using cardiopulmonary bypass: a retrospective analysis of 1386 cases. *Jpn J Surg* 1991;21:25–31.
11. Blumenthal JA, Madden DJ, Burker EJ, et al. A preliminary study of the effects of cardiac procedures on cognitive performance. *Int J Psychosom* 1991;38:13–16.
12. Stephan H, Weyland A, Kazmaier S, Henze T, Menck S, Sonntag H. Acid-base management during hypothermic cardiopulmonary bypass does not affect cerebral metabolism but does affect blood flow and neurological outcome. *Br J Anesth* 1992;69:51–57.
13. Branthwaite WA. Factors affecting cerebral activity during open heart surgery. *Anesthesia* 1973;28:619–625.
14. Patel RL, Turtle MRJ, Chambers DJ, Newman S, Venn GE. Hyperperfusion and cerebral dysfunction effect of differing acid-base management during cardiopulmonary bypass. *Eur J Cardiothorac Surg* 1993;7:457–464.
15. Solis RT, Kennedy PS, Beall AC, Noon GP, Debakey ME. Cardiopulmonary bypass microembolization and platelet aggregation. *Circulation* 1975;52:103–108.
16. Schmidt R, Fazekas F, Offenbacher H, et al. Brain magnetic resonance imaging in coronary artery bypass grafts: a pre and postoperative assessment. *Neurology* 1993; 13:775–778.
17. Messa C, Fazio F, Costa DC, Ell PJ. Clinical brain radionuclide imaging studies. *Semin Nucl Med* 1995;25:111–143.
18. Mayberg HS, Lewis PJ, Regenold W, Wagner HN. Paralimbic hypoperfusion in unipolar depression. *J Nucl Med* 1994;35:929–934.
19. Buschaum MS, De Lisi LE, Holcomb HH, et al. Anterior posterior gradients in cerebral glucose use in schizophrenia and affective disorders. *Arch Gen Psych* 1984;41:1159–1166.
20. Baxter LR, Phelps ME, Mazziotta JC, et al. Cerebral metabolic rates for glucose in mood disorders: studies with positron emission tomography and ^{18}F-fluorodeoxyglucose. *Arch Gen Psych* 1985;42:441–447.
21. Bench CJ, Scott LC, Brown RG, et al. Regional cerebral blood flow in depression determined by positron emission tomography. *J Cereb Blood Flow Metab* 1991;11: 654–657.
22. Van Heertum RL, O'Cannel R. Functional brain imaging in the evaluation of psychiatric illness. *Semin Nucl Med* 1991;21:24–39.
23. Holman BL, Johnson KA, Gerada B, Carvalho PA, Sortlin A. The scintigraphic appearance of Alzheimer's disease: a prospective study using technetium-99m-HMPAO SPECT. *J Nucl Med* 1991;33:181–185.
24. Gökgöz L, Günaydin S, Ünlü M, Boratav C, Babacan A, Inanir S. Psychiatric complications of cardiac surgery: postoperative delirium syndrome. *Scand J Thorac Cardiovasc Surg* 1997;31:217–222.
25. Holman BL, Devous MD, Sr. Functional brain SPECT: the emergence of a powerful clinical method. *J Nucl Med* 1992;33:1888–1904.
26. Roine OR, Launes J, Nikkihen P, Phil L, Lindroth L, Kaste M. Regional cerebral blood flow after human cardiac arrest. *Arch Neurol* 1991;48:625–629.
27. De Volder AG, Goffinet AM, Bol A, Michael C, Barsy T, Laterre C. Brain glucose metabolism in postanoxic syndrome. *Arch Neurol* 1990;47:197–204.
28. Taylor KM, Wright GS, Reid JS, et al. Comparative studies of pulsatile and nonpulsatile flow during cardiopulmonary bypass. The effect on adrenal secretion of cortisol. *J Thorac Cardiovasc Surg* 1978;75:574–578.
29. Taylor KM, Wright GS, Bain WH, Caves PK, Beastall GS. Comparative studies of pulsatile and nonpulsatile flow during cardiopulmonary bypass. Response of anterior pituitary gland to thyrotropin-releasing hormone. *J Thorac Cardiovasc Surg* 1978;75: 579–584.

Dual Spillover Problem in the Myocardial Septum with Nitrogen-13-Ammonia Flow Quantitation

Jens D. Hove, Sanjiv S. Gambhir, Klaus F. Kofoed, Henning Kelbæk, Heinrich R. Schelbert and Michael E. Phelps

Crump Institute for Biological Imaging, Division of Nuclear Medicine, Departments of Molecular and Medical Pharmacology and Biomathematics, University of California at Los Angeles School of Medicine, Los Angeles, California; and Division of Cardiology, Medical Department B, The Heart Center, Rigshospitalet, Copenhagen, Denmark

Conventional cardiac PET modeling techniques for [^{13}N]ammonia flow determination do not fully account for the effects of spillover of activity from the right ventricle (RV) onto the activity in the myocardial septum. The purpose of this study was to investigate and to quantitatively account and correct for this effect. **Methods:** Simulations were performed to determine the error introduced by conventional quantitation using septal time-activity curves, which only account for left ventricle (LV) spillover. Furthermore, we explored two separate methods to account for the dual spillover problem: direct estimation of the RV and LV spillover fractions incorporated into the [^{13}N]ammonia model by using the LV and RV input functions in the fit and estimation of the relative dispersion and time shift between the LV and RV input functions by fitting using only the LV input function. The simulated curves were fitted using a two-compartment [^{13}N]ammonia model. Flow estimates from the conventional model and the models including either of the two correction procedures were compared with canine microsphere data. **Results:** The influence of RV spillover on flow estimation in the septum is determined by several parameters (e.g., dispersion between the RV and LV input function). Depending on the value of these parameters, the septal flow may be underestimated by 0%–30%. The applied methods for correction of the dual spillover problem were comparable and allow for more accurate quantitation in the septum. The canine microsphere data revealed that flow underestimation in the septum is small but significant. **Conclusion:** Dual spillover in the myocardial septum can introduce significant errors in the estimation of flow by the conventional [^{13}N]ammonia model fitting method, which does not properly account for the RV spillover. Adjusting for the RV spillover in one of the two proposed methods allows for more accurate quantitation of myocardial septal flow with [^{13}N]ammonia PET data.

Key Words: PET; myocardial blood flow; septum; nitrogen-13-ammonia

J Nucl Med 1998; 39:591–598

Received Sep. 12, 1996; revision accepted Jun. 24, 1997.

For correspondence or reprints contact: Sanjiv Sam Gambhir, MD, PhD, Crump Institute for Biological Imaging, UCLA School of Medicine, A-222B CIBI, 700 Westwood Plaza, Los Angeles, CA 90095-1770.

PET is currently being used for quantitation of blood flow in the myocardium (*1–4*). Accurate quantitation requires measuring plasma (input function) and tissue time-activity curves, a tracer kinetic model and appropriate correction for resolution-related (spillover and partial volume) effects.

The term spillover describes blurring of activity from one region of interest (ROI) to another. Spillover from the left ventricle (LV) to the adjacent myocardium accounts for, on average, 10%–40% of the activity derived in the initial part of the tissue time-activity curve (*5,6*). Conventional fitting methods have accounted for this spillover effect in the fitting procedure (by estimating an additional parameter), and hence, they directly account for spillover from the LV to myocardial tissue.

Due to the anatomical position of the septum (between the right ventricle (RV) and the LV), insufficient correction of the spillover effect from the RV cavity may be expected in the septum. If the blood time-activity profile is identical in the LV and RV, the conventional fitting correction methods would account sufficiently for spillover in the septum (in this area, the spillover would approximately be twice the value of spillover in tissue that is only bordered by one blood pool). However, due to dispersion and time shift between the RV and LV input function (originating from the blood passage through the pulmonary system), the LV and RV input functions are not similar. Recent studies by Iida et al. (*7*) indicate that blood flow in the septum, estimated by the [^{15}O]CO_2 slow inhalation procedure, may be underestimated by approximately 10%–15% due to the additional spillover from the RV. In addition, studies performed by Krivokapich et al. (*8*) on human subjects demonstrated that flow values measured with [^{13}N]ammonia PET were approximately 25% lower in the septum compared to the average myocardial value.

In this study, we intended to systematically study the effect of the time shift and dispersion between the RV and LV input functions on the estimated flow with [^{13}N]ammonia studies and to develop simple and appropriate methods to correct for this dual spillover effect. Two different correction procedures were evaluated:

1. Incorporation of image-derived RV and LV input functions and estimation of RV and LV spillover fractions flow.
2. Estimation of the approximate RV input function from the image-derived LV input function by estimating dispersion and time shift between the RV and LV input functions in addition to estimating flow and spillover fractions using a [^{13}N]ammonia model (*8*).

THEORY

Spillover of activity from one region to another arises from different factors like cardiac movement, patient movement, scattering events, tomograph resolution and the effective reconstructed resolution. As shown in Figure 1, the image-derived tissue curve may be decomposed into a fraction containing the spillover and a fraction containing the pure tissue curve. Part of the superimposed activity arises from the blood pool contained in the vascular part of the myocardial tissue and not from resolution effects. The vascular volume in the myocardium has been estimated to be approximately 10% (*6,9*).

Due to time shift and dispersion, the activity profiles in the RV and LV are not generally identical. Time shift arises from the delay caused by the non-negligible transit time through the pulmonary circulation, whereas dispersion is due to effects caused by features such as the nonhomogenous velocity profile in the vessels and different transit times/pathways through the pulmonary system (*10*).

Previous studies by Iida et al. (*11*) and Meyer et al. (*12*) have shown that both time shift and dispersion are of importance in the mathematical transformation describing the changes in time-activity profiles that are observed from different measuring points in the arterial system. However, to a certain extent, compensation of a misestimation of one parameter is accomplished by an appropriate change in the other (*11*). The mathematical transform that was studied here to model the difference between the RV and LV input functions is given by Equation 1:

$$LV(t + \Delta t) = RV(t) \otimes \frac{1}{\tau} \exp\left(-\frac{t}{\tau}\right), \qquad \text{Eq. 1}$$

where Δt denotes the time shift, τ is the dispersion constant and $\otimes$ denotes the convolution operation. LV(t) and RV(t) are the time-activity profiles in the chamber of the LV and RV. By using the Laplace transform, this can be shown to be equivalent to:

$$RV(t) = LV(t + \Delta t) + \tau \cdot \dot{LV}(t + \Delta t), \qquad \text{Eq. 2}$$

where $\dot{LV}(t + \Delta t)$ denotes the time derivative of $LV(t + \Delta t)$.

NITROGEN-13-AMMONIA MODEL AND CORRECTION PROCEDURES

The two-compartment [^{13}N]ammonia model used in this work to estimate myocardial blood flow has been described in detail elsewhere (*8,13,14*). Correction for the RV spillover may theoretically be done in many different ways. In this work, we focus on two different approaches:

1. By an ROI-derived estimate of the RV input function and subsequent decomposition of the measured tissue curve into the true tissue curve and RV and LV spillover fractions:

$$A_{Measured}(t, F) = A_{True}(t, F) + SP_1 \cdot LV(t) + SP_2 \cdot RV(t) + \varepsilon(t), \qquad \text{Eq. 3}$$

where $A_{Measured}(t,F)$ denotes the measured septum time-activity curve, $A_{True}(t,F)$ is the true septal time-activity curve, LV(t) is the LV input function, τ is the dispersion, Δt is the time shift, $\varepsilon(t)$ is the noise, t is the sampling time vector ($= t_1, t_2, \ldots, t_n$), F is the blood flow [in ml/(min·g)] and SP_1 and SP_2 are the spillover coefficients. In this equation, it is assumed that the influence of other spillover sources is negligible. It is also assumed that the LV and RV input functions are error-free and that the data are corrected for any partial volume effects. Hence, implementation of this correction procedure requires identification of three parameters (F, SP_1 and SP_2), compared to two parameters in the original model (F and SP_1).

2. By characterizing the RV contribution in terms of the LV input function and incorporating the RV spillover correction in the fit. Fit = $(C_m(t)) + SP_1 \cdot LV + SP_2 \cdot g\{LV\}$. In this approach, g{LV} denotes the calculated RV input function, and by substituting the g{LV} expression given by Equation 2, the equation system is:

$$A_{Measured}(t, F) \cong A_{True}(t, F) + SP_1 \cdot LV(t) + SP_2 \cdot [LV(t + \Delta t) + \tau \cdot \dot{LV}(t + \Delta t)] + \varepsilon(t). \qquad \text{Eq. 4}$$

This correction procedure requires identification of five different parameters (F, SP_1, SP_2, Δt and τ).

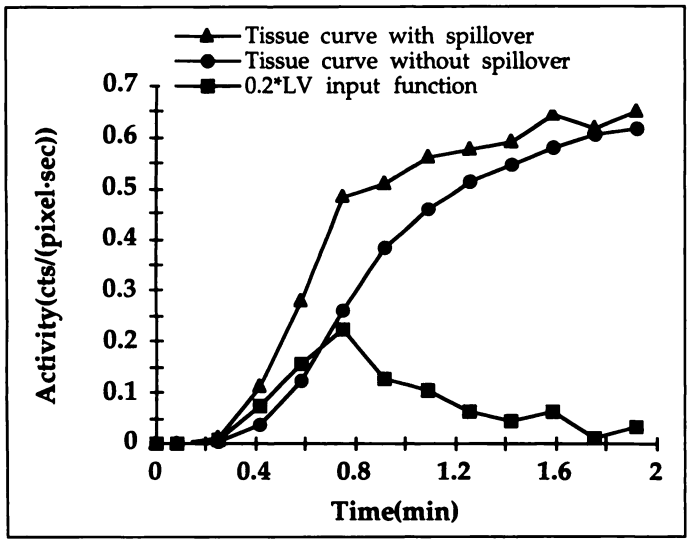

FIGURE 1. The sampled tissue time-activity curve is composed of a spillover fraction, superimposed on the true tissue time-activity curve. In the modeling procedure, the sampled curve is mathematically decomposed into its two components.

MATERIALS AND METHODS

Data Acquisition

PET. All studies were performed on a Siemens/CTI 931 positron tomograph (Des Plaines, IL), which acquires 15 transaxial images simultaneously (*15*). We used three different sets of input functions obtained from a study involving cardiac transplant recipients and nine sets from a study of adult mongrel dogs. All studies were generated according to the following protocol. In each study, [^{13}N]ammonia (740 MBq in the human studies and 555 MBq in the canine studies) was automatically injected over 30 sec followed by a 30-sec flush period, while the dynamic imaging sequence started. The dynamic acquisition consisted of 12 frames of 10 sec each, 2 frames of 30 sec each, 1 frame of 60 sec and 1 frame of 15 min. The last frame of the transaxially acquired images was reoriented into six short-axis planes (*16,17*).

Quantification of Time-Activity Curves. The same anatomical landmark (the insertion of the RV into the intraventricular septum) was used in all studies to ensure correct identification of the right cavity. The blood-pool activity on three short-axis images (one basilar, one midventricular and one apical image) was measured from a small ROI centered in the LV and RV blood pools (*18*). Similarly, the septal and inferior (chosen as a remote area with negligible RV spillover) activity was measured from a ROI that was automatically centered around the peak value in either the septum or the inferior wall (with a ROI width of approximately 4 mm). The regions were then copied to the first 120 sec of the dynamic imaging sequence to obtain the LV and RV input functions and the septum time-activity curves. The spillover values for various ROI widths in the septal part of the myocardium have been further analyzed in the Appendix.

Each time-activity curve (septal, remote, LV and RV) from the three short-axis images were averaged and corrected for physical decay. The septal and remote time-activity curve was corrected for partial volume effects assuming a uniform thickness of 10 mm, a ROI width of 4 mm and a FWHM of 10 mm (*19*). Partial volume correction for the canine studies was based on the myocardial thickness obtained from a profile fitting approach.

Right and Left Ventricle Transformation

The mathematical transformations describing the mapping between the LV and RV input functions (Eqs. 1 and 2) were validated to justify their usage in the subsequently performed simulations. We fitted an image-derived RV input function using the corresponding image-derived LV input function and fitting for time shift, dispersion and proportionality parameters.

Simulations

To investigate the effect of the actual shape of the uncorrected RV spillover on the estimated flow error, we generated tissue curves simulating spillover from fixed RV input functions (canine or human) and from LV input functions, which were generated according to Equation 1 for a wide range of parameter settings (time shift 0–6 sec; dispersion 1–20 sec).

Different total acquisition times were investigated in the range 70–180 sec. To extend the actual sampling interval (120 sec) linear interpolation was used.

The flow value was set to different values in the range between 0.7 and 4 ml/min/g, RV and LV spillover fractions ranged between 0% and 40%. Gaussian noise (s.d. in the range between 0.1% and 3% of the noise-free value weighted by the inverse of its square root) was added to the generated tissue curves and input functions to simulate real noise levels.

Tissue curves with superimposed RV and LV spillover were generated using the [^{13}N]ammonia model with different input functions (human and canine), total acquisition times and for various values of F, Δt, τ, SP_1 and SP_2. By reapplying the conventional model equations, with and without (no RV spillover correction) modifications, on the corresponding tissue/input curves, the flow values were estimated and compared to the original values. Depending on the added noise level, this procedure was repeated up to 30 times, and the generated mean flow error and s.d. were calculated. The two different correction procedures were applied to account for the additional RV spillover. A four-parameter fit was also performed with the time shift fixed in the range 0–6 sec or the dispersion fixed between 1 and 21 sec.

All simulations were performed on Apple Macintosh computers. The data were generated with the SIMPLE (Los Angeles, CA) simulation/modeling software package (*20*).

Septal Curve Analysis

Finally, measured time-activity curves from septal regions in three human and nine canine studies were analyzed with the conventional model and either the modified four-parameter (F, SP_1, SP_2 and ΔT) model (τ fixed to 12 sec) or the modified three-parameter (F, SP_1 and SP_2) model. Microsphere flow from the septal regions in the canine studies were compared with flow values obtained from the three different models. Polystyrene microspheres (15 ± 0.3 μm diameter; DuPont, Wilmington, DE) labeled with ^{103}Ru were injected into the left atrium while an arterial reference sample was simultaneously withdrawn from the descending aorta. Transmural tissue samples were counted in a well counter, and regional blood flow was calculated by the arterial reference sample technique (*21*).

Statistical Analysis

The continuous variables were expressed as means ± s.d. All statistical tests were paired, two-tailed Student's t-tests (*22*). Probability values of less than 0.05 were considered statistically significant.

RESULTS

As illustrated in Figure 2, the transformation (Eq. 2) between the LV and RV input function corrects sufficiently for the differences between these input functions. In canines, the mean values ± s.d. of time shift and dispersion were 3.8 ± 2.6 sec and 6.9 ± 2.6 sec, respectively. In human studies, the mean values ± s.d. were 1.0 ± 1.1 sec and 10.2 ± 4.2 sec.

The plot in Figure 3A displays the average flow error when three different canine RV input functions are used. As shown, the flow error increases according to the degree of dissimilarity (characterized by the dispersion) between the LV and RV input functions. The time shift is less important and actually tends to

decrease the error in the flow estimate for large dispersion values. In Figure 3B, a similar plot has been generated using human input functions for the same parameters. In this plot, the flow error values are higher, and the time shift value also has less influence on the flow estimation as compared to the canine values. Average dispersion values from human studies of approximately 10 sec correspond to a 10%–15% flow error.

The analysis of the three different human and canine input functions indicated that they are different with regard to FWHM values [LV: 33.6 ± 6.7 sec (human) compared to 20.4 ± 4.6 sec (canine); RV: 27.1 ± 2.7 sec (human) compared to 17.5 ± 2.2 sec (canine)]. Furthermore, the canine input functions tend to reach their maximal value within a shorter time than the corresponding human input functions [LV: 48.5 ± 6.1 sec (human) compared to 28.5 ± 5.6 sec (canine); RV: 45.1 ± 10.1 sec (human) compared to 21.8 ± 5.9 sec (canine)].

Figure 4 shows the effect of the total acquisition time on the flow estimation. Gaussian noise of 3% has been added to one of the simulation sequences. From Figure 4 data, it appears that a total acquisition time exceeding 100 sec can reduce the RV spillover effect significantly. We found that the actual cutoff value for this flow error reduction was dependent on each individual study. From the analyzed studies, it had a range between 90 and 120 sec. These results were fairly independent of noise added to the tissue curve and the input function.

The effect of different flow magnitudes is shown in Figure 5, in which the error of the flow estimate is plotted against the flow magnitude. The percentage flow error decreases as the flow magnitude increases. Figure 5 is based on the study of a single human input function. The other input functions gave similar results, except that the flow errors overall were smaller. The addition of noise did not change the results.

The mean percentage flow error is plotted against the RV spillover coefficient for fixed time shift (2 sec) and dispersion (13 sec) in Figure 6. Flow is increasingly underestimated (up to 30% for the selected parameters) for increasing RV spillover.

Figure 7 shows the flow error for varying degrees of RV spillover and fitting with RV spillover correction according to methods 1 and 2. Fits that included the RV input function could compensate for the flow error caused by RV spillover. The addition of noise did not change the results.

Fitting the curves sampled for 120 sec by the five-parameter approach yielded flow estimates to within 1% of the real values in the noiseless cases. The remaining four variables, however, were not numerically identifiable. With a constant dispersion value of 12 sec, fitting for flow, RV/LV spillover and time shift, the flow was estimated to within 3% of the true value. Fixing the time shift also gave flow estimates with a small error, but the convergence of the fitting procedure was slow.

In Figure 8, the septum curve from a human study is fitted according to the conventional method and according to the modified method that uses the analytical RV spillover correction term (with fixed dispersion value equal to 12 sec). As illustrated in the figure, the effect of the RV spillover correction is most significant for the early data points (time = 0.6–1.0 min). The flow estimate is 13% lower in the conventional fit. In a similar analysis of the two other studies, the flow estimates were 6% and 9% lower when RV correction was not performed.

Fits performed according to the modified three-parameter model matched flow values from the four-parameter fits to within 3%.

The canine microsphere analysis revealed that the flow values in the septal ROIs are underestimated by 0.3%–7.3% (3.0% ± 1.9%) with the conventional model compared to either the three-parameter or the four-parameter model ($p < 0.007$). In the remote area, however, the flow values from the three different methods were statistically insignificant.

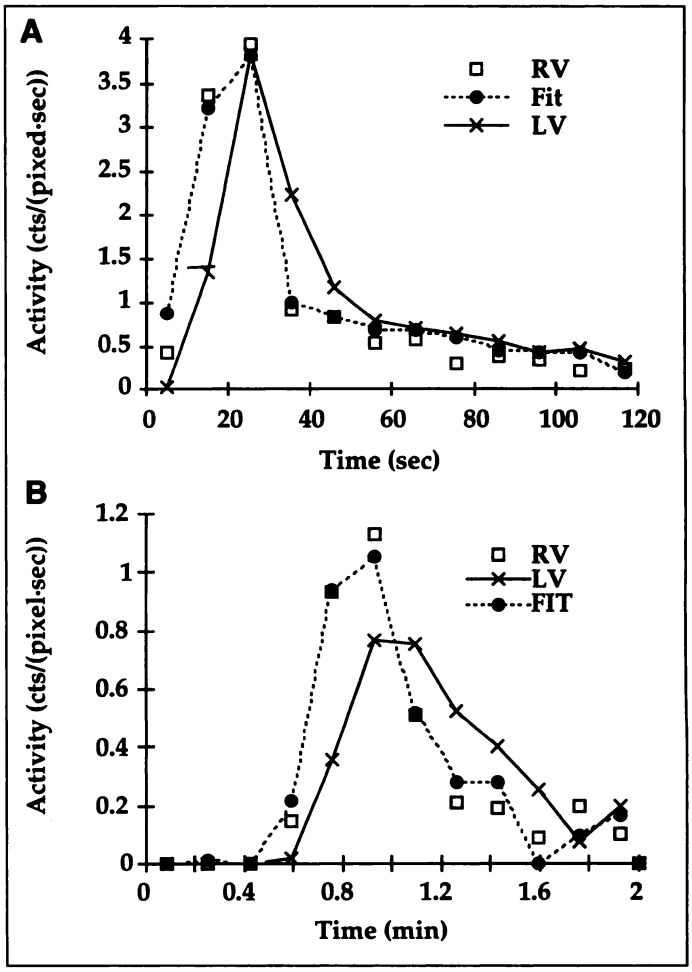

FIGURE 2. (A) Canine and (B) human studies. The RV input functions were fitted according to Equation 2 using the corresponding LV input functions with time shift and dispersion as fitting parameters. The RV and LV input functions are displayed together with the fitted RV input function (obtained from the LV input function and the time shift and dispersion parameters). In the canine study, the time shift was 2 sec, and the dispersion was 6 sec. The human study had a time shift of 2 sec and dispersion of 13 sec.

DISCUSSION

The results of this study show that estimates of flow in the septum can be underestimated by 0%–30% if the RV spillover is not properly considered. The magnitude of the RV spillover onto the ROI affects the flow estimates. With increasing amounts of RV spillover, the percentage underestimation increases as shown in Figure 6. The magnitude of the LV + RV spillover onto the septum is itself dependent on several parameters, such as the effective FWHM, septal wall thickness and ROI width and placement. Depending on these parameters, the dual spillover from the LV and RV to the septum is between 10% and 60%, as shown in the Appendix. Additional spillover from the blood pool contained in the septum accounts for approximately 10%, which has to be added to the dual spillover coefficients calculated in the Appendix. In this study, an automatic software algorithm was used to ensure appropriate positioning of the tissue ROIs. A possible misplacement of a ROI (though unlikely) would increase the spillover from the closest lying chamber while reducing the spillover from the other chamber. The total spillover would be approximately constant, but the mean ROI counts would decrease. Accurate

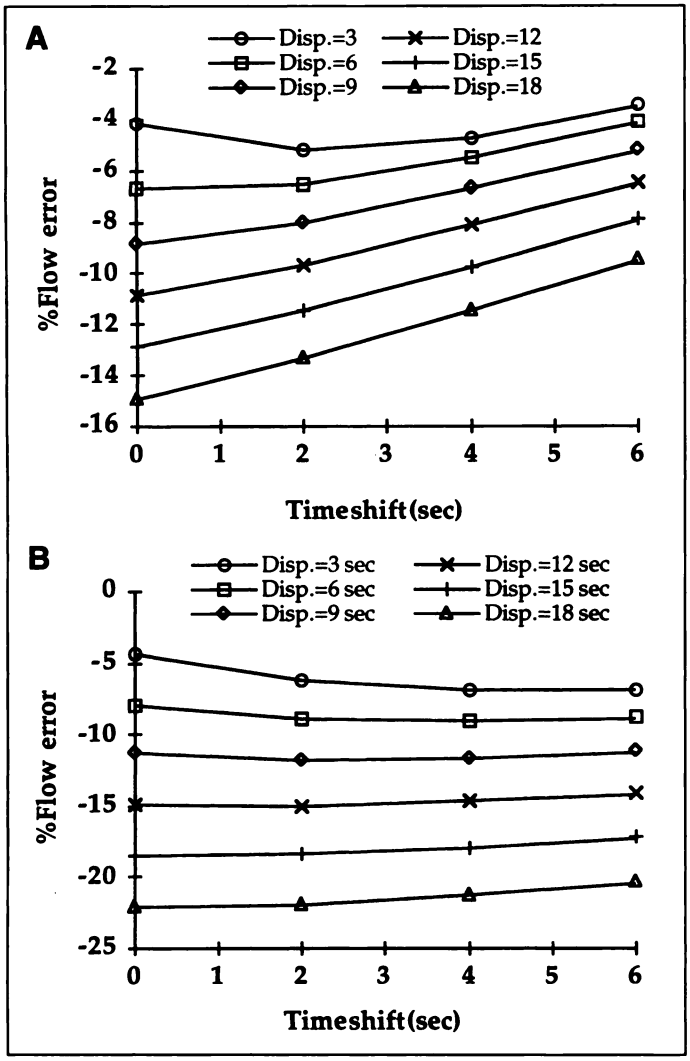

FIGURE 3. Canine (A) and human (B) studies. The average percentage flow errors from simulations with three different canine and human input functions are plotted against time shift (for various values of dispersion) between the RV and LV input functions. The plots were generated with fixed RV (0.3) and LV (0.3) spillover fractions, total acquisition time (120 sec) and flow [1 ml/(min·g)].

positioning of the ROI, as was done in this study, is critical in obtaining good estimates of flow.

Dispersion and time shift have previously been described as important factors when input functions derived at different physical sampling points are characterized. The input functions used in this study (Fig. 2) clearly show that these parameters also are of importance when dealing with input functions derived from the RV and LV. The distortion (as measured by the dispersion value) between the two input functions seems to be less pronounced in canine studies, as compared to human studies. It may be anticipated that the dispersion and time shift are considerably larger in patients with left ventricular dysfunction and elevated pulmonary outflow pressures (*23*).

The flow error is also related to the relative amount of distortion caused by the RV spillover on the septal tissue time-activity curve. The degree of distortion is best reflected by the dispersion between the RV and LV input function. Increasing time shift has a less pronounced effect and actually tends to reduce the significance of the RV spillover for larger values. This finding is due to a translation of the RV spillover curve relative to the tissue curve for increasing time shift. The true tissue curve is mainly related to the degree of trapping of tracer

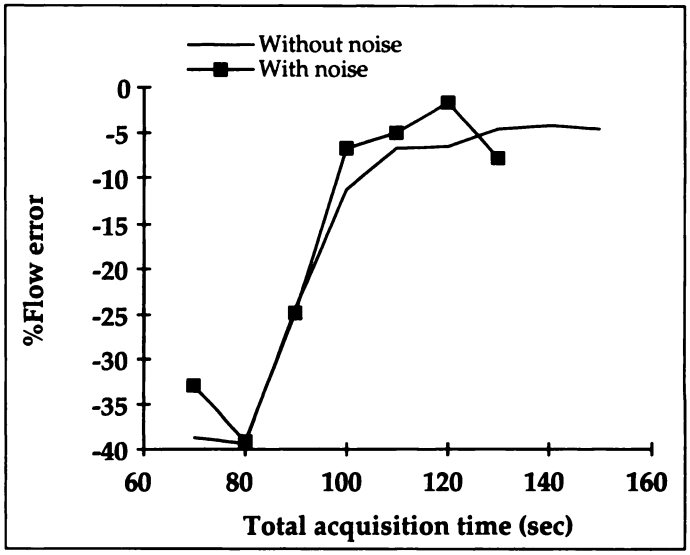

FIGURE 4. The percentage flow error is displayed as a function of the total acquisition time in seconds. The following parameters were fixed: time shift = 2 sec, dispersion = 13 sec, flow value = 1 ml/(min·g), LV spillover fraction = 0.2 and RV spillover fraction = 0.3. Gaussian noise (3%) was superimposed in one of the simulation sequences.

in tissue, and hence, it is more closely related to the LV input function, which is assumed to be equal to the tracer time-activity profile in the capillaries. If the time shift between the RV and LV input functions were sufficiently large, the RV spillover would create a spillover image on the tissue curve which would be completely separated from the true tissue curve. Thus, increasing time shift causes the number of points in the tissue curve, which are influenced by the RV spillover to decrease and, hence, the underestimation of flow decreases. This effect is more pronounced for sharply peaked input functions, which are seen in canine studies. The total spillover value used in the simulations seen in Figure 3 was 60%. This value may account for spillover seen in patients with dilated cardiomyopathy. In patients with a myocardial thickness of 10 mm, the total spillover is only anticipated to be approximately 30% (with a FWHM of 10 mm). The flow errors seen in Figure

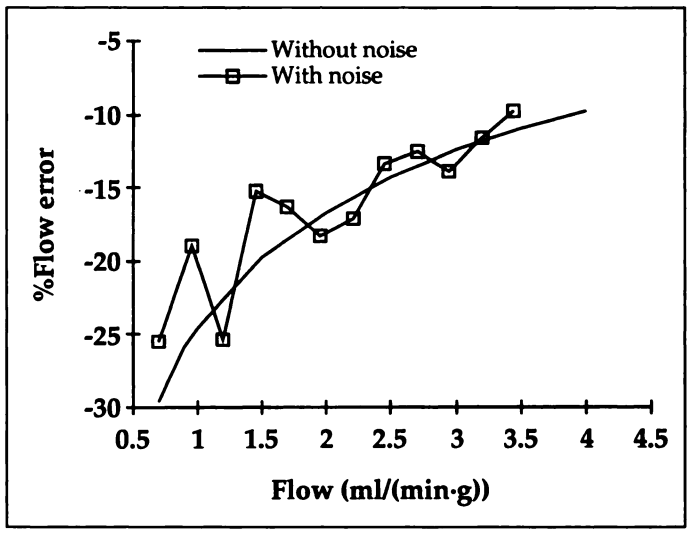

FIGURE 5. The relationship between the flow error in percent and the flow magnitude is displayed. The flow error decreases for increasing flow. Time shift = 2 sec, dispersion = 13 sec, total acquisition time = 120 sec, RV spillover = 0.3 and LV spillover = 0.2. A single human input function has been used to generate the plot. Gaussian noise of 3% was added to generate the noisy simulations.

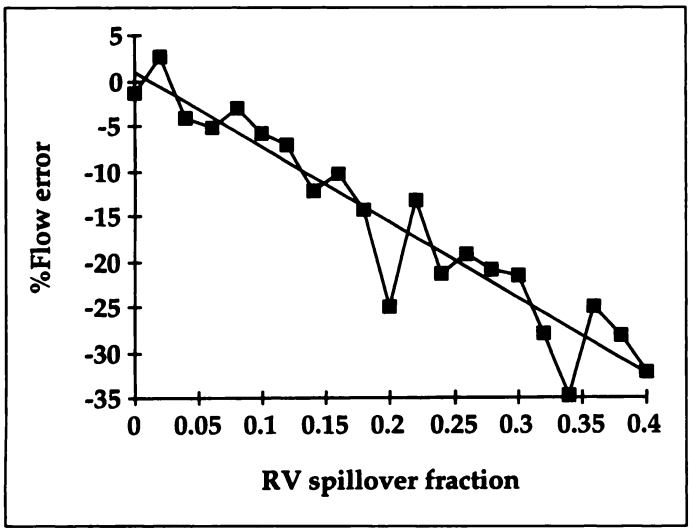

FIGURE 6. The flow error as a percentage is displayed as a function of the RV spillover fraction. The conventional model (without RV spillover correction) has been applied. Gaussian noise (1%) has been superimposed to the tissue curves and input functions. LV spillover = 0.2 and F = 1 ml/(min·g). The total acquisition time was 120 sec. An input function derived from a human study was used. Time shift was fixed to 2 sec, and the dispersion was fixed to 13 sec.

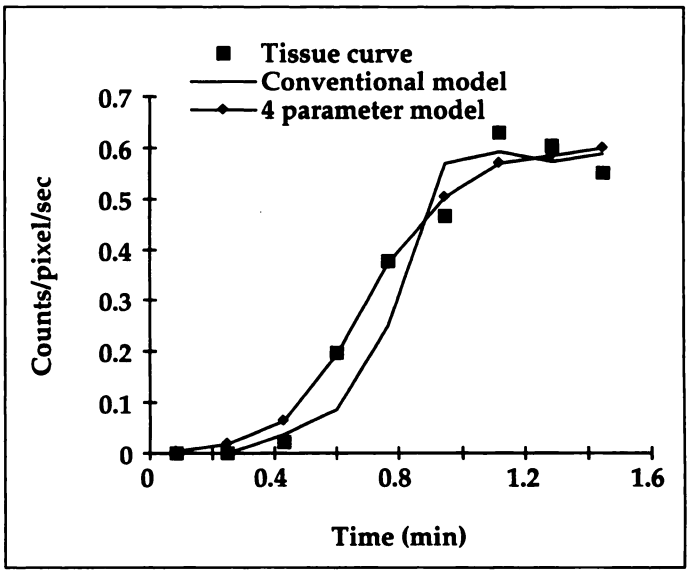

FIGURE 8. Septal tissue curves fitted according to the conventional and the modified ammonia model are displayed. In the conventional fit, the flow is estimated to 1.40 ml/min/g and the goodness of the fit is equal to 0.13, whereas the fit according to the modified four-parameter model (dispersion fixed to 12 sec) gave a flow value of 1.61 ml/min/g with a goodness of the fit value of 0.075.

3 would then be reduced accordingly to approximately 10%–15%, as seen in Figure 6.

Increasing dispersion causes the shape of the input curves to change (increasing the FWHM value) having less influence on the peak time. As the input functions become more dissimilar, correction for LV spillover alone will be increasingly inappropriate in accounting for the simultaneously occurring RV spillover.

The flow values were always underestimated to varying degrees, when there was no accounting for RV spillover. Apparently, this was due to an overestimation of the LV spillover, which was observed concurrently in most of the cases. Left ventricular spillover overestimation is related to insufficient modeling of the first part of the time-activity curve. In an attempt to correct for the initial RV spillover, the LV spillover coefficient has to be very high as the activity in the LV is low in the initial frames.

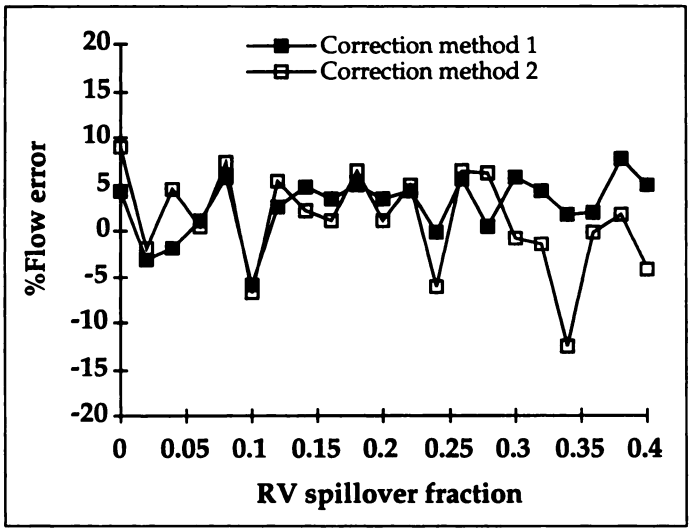

FIGURE 7. The flow error is displayed as a function of RV spillover. The model includes correction according to method 1 and the modified method 2. In the modified method 2, dispersion was fixed to 12 sec, and four parameters were estimated (F, SP_1, SP_2 and ΔT).

The shape of the input function is also related to the flow error. Sharply peaked input functions with a narrow width (as measured by FWHM) have been associated with less error for estimates of flow (*11*). Another important reason for the difference in flow estimation error between simulations with canine and human input functions (Fig. 3) is related to the number of nonaffected (by spillover) sampling points as discussed below.

The total acquisition time is important because the initial peak of the tissue curve, caused by the RV spillover, can be anticipated to be relatively more important for fewer sampling points. Different total acquisition times are used for different PET studies. In human study protocols, the usual sampling time is 120 sec, whereas the sampling interval applied for the analysis of the canine ammonia data are only 90 sec because significant amounts of ammonia metabolites have been shown to occur after this time period (*1,24*). A total acquisition time shorter than around 100 sec enhances the error introduced in the estimation of the flow parameters. When the fitting procedure is analyzed in further detail, this seems to be related to the amount of nonaffected (by spillover) data points. Total acquisition times shorter than 100 sec do not allow for accurate fitting because only the two or three endpoints are without significant influence of the blood-pool spillover. In canine studies, this effect is less pronounced as canine input functions reach their maximum early in the sampling interval compared to human input functions. In addition, they have a smaller width as seen from the FWHM values. Both factors tend to increase the number of sampling points in the tissue time-activity curve that are without significant RV spillover.

Further investigations also revealed that the number of usable tissue points was dependent on the number of blank scans in the dynamic sequence. Increasing the number of blank scans will increase the critical total acquisition time accordingly. A typical ammonia study of 12 frames includes one to three frames containing no activity due to the transit time between the site of injection and the RV. The number of blank scans in the study used to derive Figure 4 was one. Hence, the value of 100 sec in Figure 4 may increase to 120 sec if the number of blank scans

is increased from one to three. Additionally, it may decrease to 90 sec if the study is without any blank scan. This probably explains why the critical value of the total acquisition time was study-dependent.

The flow error decreases with increasing flow. The reason for this finding is related to increased initial tracer uptake rate for increasing flow, causing the fixed spillover fraction to be less significant for higher flow values.

Correction method 2 fits for five different parameters. However, when fitting a curve with only nine sampling points (the shorter sampling intervals), the mathematical determination of five parameters is ill-defined because the number of points to be fitted has to be greater than twice the number of parameters to be estimated (*25*). Applying more than 10 data points (in our case, using a total acquisition time of 120 sec and restricting the number of blank scans to be less than two), the flow is well estimated. However, the remaining four parameters are not numerically identifiable. Fitting for four parameters with fixed time shift, the flow estimate became stable within two to four cycles, whereas τ and SP_2 were adjusted in opposite directions. This may be related to the $\tau \cdot SP_2$ product, which appears in Equation 4.

Both correction methods could reduce the flow error in the human studies. The time-activity profile in the RV PET images needs to be experimentally compared with the activity measured directly from RV. Theoretically, the image-derived RV input function may suffer from problems due to late septum to RV spillover, which is expected to distort the late part of the input function, thereby making the ROI correction method less suitable. A possible way of avoiding this problem is to use an input function derived from the right atrium. The correction method which only requires the LV input function may be preferable until the RV or the right atrium input function has been further validated. Other approaches, such as factor analysis, may also be useful in correcting for the dual spillover problem and are currently being explored.

This work is based on a two-compartment ammonia model. The three-compartment ammonia model (*1*) will also be affected by dual spillover in the septum, but the flow estimation may be more or less sensitive to the RV spillover compared to the model analyzed in the present work. Hutchins et al. (*1*) did not report any significant difference between flow estimates in the septum and other areas, whereas Krivokapich et al. (*8*) (using the same model as in this study) reported septal flow values that were 25% lower in the septum than the average myocardial value. Future studies will have to be performed to compare the different ammonia models with respect to the dual spillover problem.

The analysis of the human studies (Fig. 8) confirms our postulates about the effect of RV spillover and the results of our simulations. Flow tends to be underestimated if RV spillover is not considered.

The canine microsphere analysis revealed that flow estimates from the conventional model are significantly lower in the septal area compared to estimates from the three and four parameter models. Furthermore, the flow underestimation was not significant in the remote area, lending evidence that the dual spillover effect is real. The absolute size of the underestimation in the canine studies was between 0 and 7%. The relatively small underestimation seen in the canine studies may be due to factors reducing the dual spillover problem in canine versus human studies, which have been discussed previously, and the considerable thickness of the canine myocardium, which reduces the amount of RV spillover. As seen from the analysis of the human data, the flow error may be larger in human studies. Future studies will be required to further evaluate the magnitude of flow underestimation in patients and normals. Because many different parameters can effect the degree of underestimation of flow, it is useful to fit with the more generalized model to properly account for the RV spillover, even if in a particular patient the magnitude of flow underestimation may be small.

CONCLUSION

This study indicates that quantitation of the myocardial blood flow with the [^{13}N]ammonia model in the interventricular septum may be underestimated by 0%–30% due to improper accounting for RV spillover. The flow error caused by the RV spillover is related to the dispersion and time shift between the RV and LV input functions, effective image resolution, septal wall thickness, ROI size and position, total acquisition time and flow value. Correction may be done either by using an ROI-derived RV input function and fitting for flow and LV and RV spillover coefficients or by fitting time shift and RV spillover, together with LV spillover and flow, while using only the LV input function.

ACKNOWLEDGMENTS

This work was presented in abstract form at the 1995 Computer and Instrumentation Council Young Investigator Competition at the Society of Nuclear Medicine Annual Meeting in Minneapolis, MN, June 12–15, 1995. This work was partially supported by funding from Department of Energy Contract DE-FC03-87ER60615. Jens D. Hove was supported in part by a scholarship from the Georg Bestles Foundation. We are grateful for professor Stig Haunsø's help. We also thank Ron Sumida, Larry Pang and Francine Aguilar for technical assistance, Drs. Carl Hoh and Magnus Dahlbom for many fruitful discussions and Theresa Sama and Diane Martin for help with the manuscript and figures.

APPENDIX

In this section, we derive the approximate spillover (from the LV and RV) to a ROI centered in the septum. The LV and RV are treated as two infinitely long bars each of width 2R separated by the myocardial septum which is treated as an infinitely long bar of width 2d. There is assumed to be homogeneous true activities C_b in the LV and RV and activity C_m in the myocardial wall. The image activity at some point x (AI(x)) is equal to the convolution of the true activity with the point spread function (*5*). From these assumptions, and given $R \gg s$ (where s is the s.d. of the point spread function, s = FWHM/2.355), the spillover coefficient may be derived as (*6*):

$$SP_{LV} = \frac{1}{2}\left[1 - ERF\left(\frac{d}{\sqrt{2}\,s}\right)\right] \qquad \text{Eq. A1}$$

Assuming symmetry, the RV spillover coefficient will be the same for a perfectly centered ROI. For a perfectly centered ROI with a width of w, the dual spillover (SP_{LV+RV}) is then given by:

$$SP_{LV+RV} = \frac{1}{2w}\int_{-\frac{w}{2}}^{\frac{w}{2}}\left(1 - ERF\left(\frac{d + x}{\sqrt{2}\,s}\right)\right)dx \qquad \text{Eq. A2}$$

Dual spillover values for different ROI geometries and wall thickness are shown in Table A-1. An effective FWHM of 12 mm yields values between 0.18 and 0.58. These estimates are only approximately valid for $R \gg s$ and for ROIs centered in the septum.

TABLE A-1
Total Spillover Values for Different Region of Interest Geometry and Wall Thickness (FWHM = 10 mm)

Spillover value	Wall thickness		
	6 mm	10 mm	14 mm
Centered ROI (width = 4mm)	0.50	0.26	0.11
Full wall ROI	0.51	0.34	0.18

Further details for the one-dimensional and two-dimensional geometries can be found in Gambhir (*5*).

REFERENCES

1. Hutchins GD, Schwaiger M, Rosenspire KC, Krivokapich J, Schelbert H, Kuhl DE. Noninvasive quantification of regional blood flow in the human heart using ^{13}N ammonia and dynamic positron emission tomographic imaging. *J Am Coll Cardiol* 1990;15:1032–1042.
2. Muzik O, Beanlands RSB, Hutchins GD, Mangner TJ, Nguyen N, Schwaiger M. Validation of nitrogen-13-ammonia tracer kinetic model for quantification of myocardial blood flow using PET. *J Nucl Med* 1993;34:83–91.
3. Nitzsche EU, Choi Y, Czernin J, Hoh CK, Huang SC, Schelbert HR. Noninvasive quantification of myocardial blood flow in humans. A direct comparison of the [^{13}N]ammonia and the [^{15}O]water techniques. *Circulation* 1996;93:2000–2006.
4. Czernin J, Müller P, Chan S, et al. Influence of age and hemodynamics on myocardial blood flow and flow reserve. *Circulation* 1993;88:62–69.
5. Gambhir SS. Quantitation of the physical factors affecting the tracer kinetic modeling of cardiac positron emission tomography data [PhD thesis]. Los Angeles: University of California at Los Angeles; 1990.
6. Henze E, Huang SC, Ratib O, Hoffman EJ, Phelps ME, Schelbert HR. Measurement of regional tissue and blood-pool radiotracer concentrations from serial tomographic images of the heart. *J Nucl Med* 1983;24:987–996.
7. Iida H, Takahashi A, Tamura Y, Ono Y, Lammertsma A. Myocardial blood flow: comparison of oxygen-15-water bolus injection, slow infusion and oxygen-15-carbon dioxide slow inhalation. *J Nucl Med* 1995;36:78–85.
8. Krivokapich J, Smith GT, Huang SC, et al. Nitrogen-13-ammonia myocardial imaging at rest and with exercise in normal volunteers: quantification of absolute myocardial perfusion with dynamic positron emission tomography. *Circulation* 1989;80:1328–1337.
9. Frank JS, Langer GA. The myocardial interstitium: its structure and its role in ionic exchange. *J Cell Biol* 1974;60:586–601.
10. Zierler KL. *Circulation times and the theory of indicator-dilution methods for determining blood flow and volume.* Baltimore: Waverly Press; 1962:585–615.
11. Iida H, Kanno I, Miura S, Murakami M, Takahashi K, Uemura K. Error analysis of a quantitative cerebral blood flow measurement using $H_2{}^{15}O$ autoradiography and positron emission tomography, with respect to the dispersion of the input function. *J Cereb Blood Flow Metab* 1986:536–545.
12. Meyer E. Simultaneous correction for tracer arrival delay and dispersion in CBF measurements by the $H_2{}^{15}O$ autoradiographic method and dynamic PET. *J Nucl Med* 1989;30:1069–1078.
13. Smith GT, Huang SC, Nienaber CA, Krivokapich J, Schelbert HR. Noninvasive quantification of regional myocardial blood flow with ^{13}N ammonia and dynamic PET [Abstract]. *J Nucl Med* 1988;29:940.
14. Kuhle W, Porenta G, Huang SC, et al. Quantitation of regional myocardial blood flow using ^{13}N-ammonia and reoriented dynamic positron emission tomographic imaging. *Circulation* 1992;86:1004–1017.
15. Spinks TJ, Jones T, Gilardi MC, Heather JD. Physical performance of the latest generation of commercial positron scanner. *Trans Nucl Sci* 1988;35:721–725.
16. Kuhle W, Porenta G, Huang SC, Phelps M, Schelbert H. Issues in the quantitation of reoriented cardiac PET images. *J Nucl Med* 1992;33:1235–1242.
17. Porenta G, Kuhle W, Czernin J, et al. Validation of PET-acquired functions for cardiac studies. *J Nucl Med* 1988;29:241–247.
19. Gambhir SS, Schwaiger M, Huang SC, et al. Simple noninvasive quantification method for measuring myocardial glucose utilization in humans employing positron emission tomography and fluorine-18-deoxyglucose. *J Nucl Med* 1989;30:359–366.
20. Gambhir SS, Mahoney DK, Huang SC, Phelps ME. Symbolic interactive modeling package and learning environment (SIMPLE): a new easy method for compartmental modeling. *Proc Soc Computer Simulation* 1996:173–186.
21. Heymann MA, Payne BD, Hoffman JIE, Rudolph AM. Blood flow measurements with radionuclide-labeled particles. *Prog Cardiovasc Dis* 1977;20:55–79.
22. Altman DG. *Practical statistics for medical research.* London: Chapman and Hall; 1991:189–191.
23. Lewis ML, Caterina RD, Giuntini C. Distribution function of transit times in the human pulmonary circulation. *J Appl Physiol* 1994;76:1363–1371.
24. Rosenspire K, Schwaiger M, Mangner T, Hutchins G, Sutorik A, Kuhl D. Metabolic fate of ^{13}N ammonia in human and canine blood. *J Nucl Med* 1990;31:163–167.
25. Mesterton-Gibbons MA. *Concrete approach to mathematical modeling.* Redwood City, CA: Addison-Wesley; 1989.

Direct Detection of Regional Myocardial Ischemia with Technetium-99m Nitroimidazole in Rabbits

Howard Weinstein, Christopher P. Reinhardt and Jeffrey A. Leppo

Departments of Nuclear Medicine and Medicine, Myocardial Isotope Research Lab, University of Massachusetts Medical Center, Worcester, Massachusetts

Conventional perfusion scintigraphy assesses disparities in regional myocardial blood flow but does not directly detect hypoxic tissue. Nitroimidazoles labeled with positron-emitting radionuclides have recently shown promise as direct markers of myocardial hypoxia. This study evaluates a new ^{99m}Tc-labeled nitroimidazole of potential benefit in standard myocardial scintigraphy. **Methods:** Technetium-99m-labeled nitroimidazole was administered to rabbits during the early reperfusion phase after 10 min (Group 1) or 60 (Group 2) min of coronary occlusion or after 10 min of a fixed coronary occlusion (Group 3). Tracer retention at 1 hr was assessed in relation to microsphere-determined blood flow during coronary occlusion and at tracer injection. The pattern of nitroimidazole retention on autoradiographs was then compared with the pattern of myocardial hypoperfusion defined by fluorescein photography to precisely define tracer localization. **Results:** The retention of nitroimidazole in Group 1 rabbits (brief occlusion) was independent of both occlusion and reperfusion blood flow and was uniformly distributed on the autoradiographs. In contrast, nitroimidazole retention in Groups 2 and 3 increased with the severity of hypoperfusion during the occlusion phase and precisely delineated the ischemic zone on all autoradiographs. **Conclusion:** This ^{99m}Tc-labeled hypoxia-avid tracer delineates severe ischemia even after blood flow to the compromised myocardium has been restored. This class of compounds can potentially enhance the physiological assessment of patients with ischemic heart disease.

Key Words: myocardial tracers; ischemia; technetium-99m nitroimidazole

J Nucl Med 1998; 39:598–607

Received Nov. 5, 1996; revision accepted Jul. 16, 1997.

For correspondence or reprints contact: Howard Weinstein, MD, University of Wisconsin, Milwaukee Clinical Campus, 960 N. 12th St., Milwaukee, WI 53233.